Physical Insight into Hypermixer Injector Design for Fuel/Air Mixing Enhancement in Scramjet Engines

Hideaki Ogawa[1]
RMIT University, Melbourne, VIC 3001, Australia

Masatoshi Kodera[2]
Japan Aerospace Exploration Agency, Kakuda, Miyagi 981-1525, Japan

Efficient mixing of fuel and air is a major objective for the successful operation of scramjet engines, where the supersonic combustion process must occur within an extremely short time frame in the hypersonic flight. This paper presents the insights gained into the key design factors and underlying mechanism for fuel/air mixing enhancement with streamwise vortices introduced by alternating wedges called hypermixers. The results of a parametric numerical study and sensitivity analysis suggest that: Narrow spanwise intervals between the alternating wedges and large fuel/air equivalence ratios are beneficial for effective mixing, while higher total pressure recovery is associated with shallower ramp angles and lower fuel/air equivalence ratios. Higher fuel penetration is achieved with steeper ramp angles and higher fuel/air equivalence ratios. Streamwise vortex circulation increases with wider spanwise spacing and steeper ramp angles, but effective mixing enhancement is observed only in the latter case.

I. Introduction

Hypersonic airbreathing propulsion offers the great potential for reliable, reusable and economical systems for access-to-space and high-speed atmospheric cruise for both civilian and strategic

---

[1] Senior lecturer, School of Aerospace, Mechanical and Manufacturing Engineering, AIAA Member
[2] Associate senior researcher, Research Unit IV, Research and Development Directorate, AIAA Member

Nomenclature

s = spanwise scaling factor of alternating wedges

θ = ramp angle of alternating wedges [°]

Φ = fuel/air equivalence ratio

M = Mach number

$\dot{m}$ = mass flow rate [kg/m^2·s]

c_χ = mass fraction of species χ

c_χ^s = stoichiometric mass fraction of species χ

η_m = mixing efficiency [%]

$\eta_m \times \Phi$ = absolute mixing quantity [%]

p_0 = total pressure [Pa]

p_{01} = total pressure at entrance [Pa]

Δp_0 = total pressure loss [Pa]

$\Delta p_{0\,STA}$ = stream-thrust averaged total pressure loss [Pa]

h_p = maximum fuel penetration height [m]

ω_x = streamwise vorticity [1/s]

Γ = streamwise vortex circulation [m^2/s]

S_i = first-order sensitivity index

S_{T_i} = total-effect sensitivity index

A = cross section

x = streamwise coordinate [m]

x' = streamwise coordinate relative to wedge tailing edge [m]

y = vertical coordinate [m]

z = spanwise coordinate [m]

Δs_{min} = minimum cell spacing [m]

purposes. Scramjet (supersonic combustion ramjet) propulsion, in particular, is a promising technology that can enable efficient and flexible transport systems by removing the need to carry oxidizers and other limitations of conventional rocket engines. The last decade has seen significant milestones in the research and development of scramjet engines: the world's first in-flight supersonic combustion in the HyShot II Program in July 2002[1], the fastest atmospheric flights recorded by NASA's X-43A scramjet-powered vehicles in the Hyper-X program at Mach 6.8 (March 2004) and

9.6 (November 2004)[2], and the recent flight by the Boeing X-51A WaveRider, which recorded the longest scramjet burn duration of 140 seconds in May 2010[3]. An axisymmetric configuration with internal compression has been explored in the SCRAMSPACE program as an international collaboration led by The University of Queensland in Australia[4]. Supersonic combustion has also been the focal point of the major European scramjet technology projects undertaken in the LAPCAT program[5].

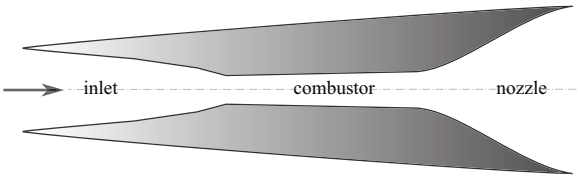

Fig. 1 Schematic of axisymmetric scramjet engine.

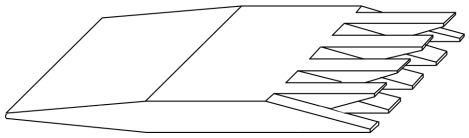

Fig. 2 Alternating-wedge type hypermixer[9].

A scramjet engine typically consists of an inlet, combustor, and nozzle, as schematically shown in Fig. 1 (the isolator section is not included in the diagram for the axisymmetric configuration presented here, which operates at relatively high Mach numbers 8+, based on upstream fuel injection and radical farming concepts[6]). It operates in a sequential process comprising flow compression, combustion and expansion. Fuel/air mixing plays a crucial role in the scramjet combustion process (fuel injection, mixing, ignition and combustion), which must occur within an extremely short residence time in hyper-velocity flowfields. A variety of fuel injection techniques have been contrived and examined in order to improve the mixing performance. Examples include: transverse/tangential injection through wall orifices/slots[7, 8], streamwise vortices with hypermixers[9–11], and fuel supply through porous media[12].

Hypermixers using alternating-wedge (AW) struts (Fig. 2), in particular, are capable of generating streamwise vortices to enhance fuel/air mixing in the core flow, incurring minimum influence of fluid compressibility[9], in contrast to the other methods which supply fuel without producing strong vorticity. Experimental and numerical studies have been conducted extensively at JAXA Kakuda Space Center in order to investigate the effects of streamwise vortices introduced by hypermixers on fuel mixing and combustion enhancement[10, 11]. These preceding studies were conducted

with primary focus on the fundamental physics of supersonic mixing and combustion due to hypermixer injectors, aiming to apply this type of injector to the scramjet combustor. The flowfield introduced by AW struts represents substantial complexity with highly coupled aerodynamic and aerothermal interactions. It therefore requires careful design based on further understanding of the underlying flow physics and key design factors. The present research is thus undertaken in order to systematically investigate the effects of the design parameters of hypermixers on the flowfields and mixing performance by means of CFD (computational fluid dynamics) simulations in conjunction with surrogate modeling used in multi-objective design optimization.

A parametric numerical study is conducted in the present research in order to examine the flowfields with various combinations of the primary hypermixer design parameters, namely the spanwise spacing, ramp angle of the wedges, and fuel/air equivalence ratio. Their influence on the mixing performance is evaluated with respect to various efficiency parameters by applying sensitivity analysis based on surrogate models to the flow properties of the mixed gas (hydrogen and air). This paper presents knowledge on the key design factors and insights into the underlying mechanisms for fuel/air mixing enhancement with hypermixers, obtained as a result of this numerical investigation.

II. Approaches

A. Configurations

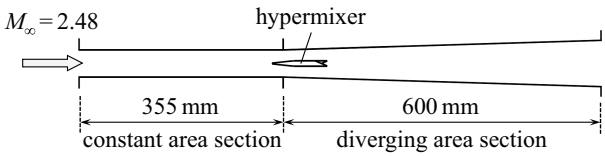

Fig. 3 Schematic of hypermixer positioned in combustor[10].

The hypermixer geometry used for the calculations is a direct-connect supersonic combustor with the AW strut fuel injector, which has been examined in JAXA Kakuda Space Center[10]. It consists of three components: (a) The front part is a 41 mm-long wedge inclined at 5.7° half angle with a leading-edge radius of 1 mm. (b) The middle part is a straight section of 44.6 mm in length and 10 mm in thickness. (c) The rear part comprises ramps inclined at a certain angle (which is 36° for the baseline geometry and varied in the parametric study) with a 1 mm-thick backward-

facing step at the trailing edge. This rear section is composed of five downward and four upward expansion ramps alternately arranged in the spanwise direction with a constant interval (which is 11 mm for the baseline geometry and varied in this study), as seen in Fig. 2. The opposite surfaces of ramps are flat and parallel to the incoming freestream. This configuration can generate eight alternate counter-rotating streamwise vortices. A circular fuel injector orifice with a diameter of 3.5 mm is placed at the intersection between the neighboring ramps, from which the fuel is injected downstream parallel to the freestream, so that the fuel is directly introduced into the center of the streamwise vortices. The combustor consists of a constant cross-sectional area chamber of 355 mm in length with an entrance height of 50 mm, followed by a 600 mm-long section with a diverging angle of 1.72°, as schematically depicted in Fig. 3. Its width is constant at 100 mm, accommodating a row of alternate ramps, whose number varies, depending on the spanwise scaling of the ramps (*e.g.*, 9 for the baseline geometry). The strut is placed at the middle of the combustor height. The strut leading edge, center of the fuel orifice and trailing edge are located at 220 mm, 312.5 mm and 318 mm downstream of the combustor entrance, respectively, for the baseline geometry (the upstream end of the combustor is directly connected with the downstream end of the nozzle section of the wind tunnel in the experimental setup).

B. Conditions

The freestream Mach number, total temperature and total pressure assumed in this study are 2.48, 2250 K and 1 MPa, respectively, corresponding to Mach 8 flight conditions for a generic scramjet engine. These nominal flow conditions are summarized in Table 1. The incoming air is vitiated, containing H_2O or OH radicals with the composition shown in Table 2, in order to attain high total temperatures by combustion of H_2 and O_2 in the experimental facility. This gas composition remains constant throughout the flowfield due to the absence of chemical reactions assumed in the present study. These freestream conditions are imposed as the inflow conditions at the combustor entrance located at $x = 190$ m (see Section II E for the definition of the coordinates). Non-slip condition is imposed only on the strut wall, while slip condition is imposed on top and bottom walls of the combustor (*i.e.*, ceiling and floor of the computational domain). Mirror (symmetry) condition

is applied to both the spanwise boundaries. The wall temperature is set to be constant at 550 K. The fuel is gaseous hydrogen at room temperature (243.6 K), being injected at the sonic speed at various pressures to achieve the intended fuel/air equivalence ratio varied in this study. Central injection is employed for fuel supply, where hydrogen is injected through a cylindrical duct bored into the wedges at the intersection between the neighboring upward and downward ramps.

Table 1 Freestream conditions

Mach number	2.48
velocity	1836 m/s
density	0.1355 kg/s
static pressure	58 kPa
static temperature	1329 K
total pressure	1 MPa
total temperature	2250 K

Table 2 Air composition (mass fraction)

O_2	0.263
H_2O	0.211
OH	0.002
N_2	0.524

C. Performance parameters

The four measures (with two auxiliary parameters) described below are selected and employed to assess the efficiency and performance of fuel/air mixing achieved with respective hypermixer configurations. Evaluation with respect to these measures is performed at the exit of the computational domain located at $x = 405$ mm. This is 92.5 mm downstream of the center of the fuel injection orifice where the distributions of the injected fuel and air form a well-defined pattern as a result of convective mixing.

- Mixing efficiency

  The mixing ability of the injectors is evaluated by the mixing efficiency defined as:

$$\eta_m \equiv \frac{1}{\dot{m}_{H_2}} \int_x \min\left(c_{H_2}, \frac{c^s_{H_2}}{c^s_{O_2}} c_{O_2}\right) d\dot{m} \tag{1}$$

  where $\dot{m}$ is the mass flow rate and c is the mass fraction. The superscript s denotes the stoichiometric values, *i.e.*, $c_{H_2} = 0.029$ and $c_{O_2} = 0.228$, which represent the ratio of fuel (hydrogen) to oxygen needed to completely burn all the available fuel. This parameter serves as an indicator of the fraction of the fuel to be consumed when all mixed gases react. However,

it inherently yields higher values for lower fuel/air equivalence ratio Φ by definition. The absolute mixing quantity $\eta_m \times \Phi$ is introduced additionally in order to allow fairer comparison across various Φ values.

- Total pressure recovery

  High total pressure recovery is a desired feature in fuel mixing because any loss in the total pressure directly leads to thrust penalty, and it is evaluated in terms of the total pressure loss defined as:

$$\Delta p_0 \equiv 1 - \frac{\int_x p_0 d\dot{m}}{\int_{x=0} p_{01} d\dot{m}} \tag{2}$$

  where p_{01} and p_0 denote the total pressure at the entrance and exit of the computational domain, respectively. The mass-averaged total pressure on which this measure is based, however, inherently does not satisfy the conservation laws. The following parameter based on the stream-thrust-averaged total pressure[13, 14] (denoted as $p_{0\,STA}$) is additionally introduced to quantify the total pressure loss, while accounting for the mass, momentum and energy on the slice plane from the three-dimensional solutions:

$$\Delta p_{0\,STA} \equiv 1 - \frac{p_{0\,STA}}{p_{01\,STA}} \tag{3}$$

  where $p_{01\,STA}$ is the stream-thrust-averaged total pressure at the entrance ($x = 0\,\mathrm{mm}$) and $p_{0\,STA}$ is that at the streamwise station of interest.

- Fuel penetration

  The extent of fuel penetration into the core flow is another useful indicator for fuel/air mixing. This criterion is assessed by the distance from the centerline of the injector orifice to the height where the hydrogen mass fraction of the jet plume reduces to 10% of the stoichiometric mass fraction, defined as:

$$h_p \equiv \max\left(z\,|_{c_{H_2} > 0.1 c^s_{H_2}}\right) \tag{4}$$

  where z denotes the vertical coordinate and $c^s_{H_2}$ the stoichiometric mass fraction of hydrogen.

- Streamwise vortex circulation

  The streamwise vortex circulation is used as the last metric to account for the overall effects of

the streamwise vorticity ω_x, which plays a primary role in the fuel/air mixing[15, 16], defined as:

$$\Gamma \equiv \int_x |\omega_x| dA \tag{5}$$

This parameter is of particular interest in examining the streamwise vorticity effects on near-field mixing, where the circulation of the streamwise vortices predominantly affects the large-scale convective mixing through the interaction between the streamwise vortices and fuel jet, as reported in References [10, 11].

D. Computational fluid dynamics

Numerical simulations are performed by using an unstructured grid-based chemical reacting code, which has been utilized extensively in computing scramjet flowfields at JAXA. It solves the three-dimensional conservation equations of mass, momentum, energy, and species concentrations[17]. The numerical method is based on a finite volume cell vertex scheme along with the LU-SGS implicit time integration algorithm[18] combined with the diagonal point implicit method to ensure both efficiency and robustness. In addition, unstructured hybrid grids are employed as mentioned in the following section. The AUSM-DV scheme[19] is applied to the calculation of inviscid flux with the second-order spatial accuracy achieved by linear reconstruction of the primitive variables inside the control volume, while central differencing is adopted for the calculation of the viscous flux. Computations are performed without turbulence models in this research because simulations with a RANS turbulence model were found to be too dissipative to clearly capture the large-scale vortex structures and dynamics in the interactions between the streamwise vortices and fuel jet, which dominate the mixing process in the downstream vicinity of the injector[20]. Non-reacting (hence chemically frozen) flow is assumed to allow investigation focusing on the mixing process dominated by vortex interactions, ruling out the influence of other factors. To achieve efficient convergence, local time stepping with a CFL (Courant-Friedrichs-Lewy) number of 10 is adopted as well as parallel computation using a METIS-based grid partitioning method and MPI (Message Passing Interface).

E. Computational mesh

Displayed in Fig. 4 is the computational mesh for the baseline geometry. The coordinate system consists of the x, y and z axis in the streamwise, vertical and spanwise directions, respectively. The origin is located on the left lateral plane (viewed from upstream) at the mid height of the combustor entrance plane, and the x axis passes through the centerline of the downward expansion ramp of the strut. The computational domain lies in a range from $x = 190\,\mathrm{mm}$ to $405\,\mathrm{mm}$, only containing a single streamwise vortex bounded between the $z = 0\,\mathrm{mm}$ and $z = 11\,\mathrm{mm}$ planes for the baseline geometry.

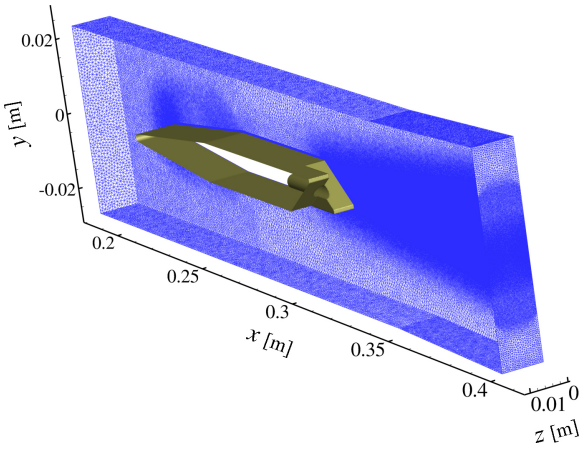

Fig. 4 Computational grids with nominal mesh resolution (baseline geometry).

The computational mesh mostly consists of tetrahedron grids generated by executing Glyph scripts in a commercial mesh generator Pointwise[21], while prismatic layers are added to the vicinity of the strut wall with the assistance of a grid generator MEGG3D[22] so as to resolve the boundary layer accurately. The grid spacing is largely uniform at $0.25\,\mathrm{mm}$ inside the domain of streamwise vortices, while it becomes coarser outside. The minimum spacing normal to the wall is $10^{-5}\,\mathrm{m}$ on the strut surface, which results in an area-averaged non-dimensionalized z^+ value of 3.5. The total number of grid points is approximately 4.3 million for the baseline geometry.

A preliminary mesh sensitivity study has been performed to investigate the influence of the mesh resolution on the flowfield, with particular attention to the mixing behavior downstream of injection, so as to examine the grid convergence. The flowfields with the baseline geometry are compared between the nominal mesh resolution and a modified one with the grid spacing inside the streamwise

vortex domain reduced to 0.125 mm, which is called "fine mesh", comprising approximately 22 million grid points (the computational mesh in the upstream domain is kept the same as the nominal one, which adequately resolved the upstream flowfield in close agreement with the experimental result[23]). Figure 5 compares the distributions of the fuel mass fraction obtained with the baseline and fine meshes at a fuel/air equivalence ratio of unity ($\Phi = 1$), plotted on streamwise planes ranging from $x = 325$ mm to 405 mm at an interval of 20 mm.

The mesh resolution appears yet to be converged quantitatively, particularly regarding the fuel concentration in the streamwise vortex cores due presumably to the effects of numerical dissipation (calculations with the fine mesh resolution have commonly been associated with flow unsteadiness and asymmetry, but flowfields developed over adequately large time steps have been used for evaluation within the resource allowance in this study). The values of the performance parameters in Table 3 show rather minor difference between the two mesh resolutions, while the fine mesh is commonly associated with slightly lower values for most parameters. On the whole qualitative agreement can be seen in the fuel distributions in Fig. 5 with respect to the streamwise vortex patterns, which are closely related to the fuel distributions and their downstream evolution[16, 24]. Therefore the nominal mesh resolution is adopted for all simulations performed in the present study to allow reasonable discussions within the limitation of computational resources.

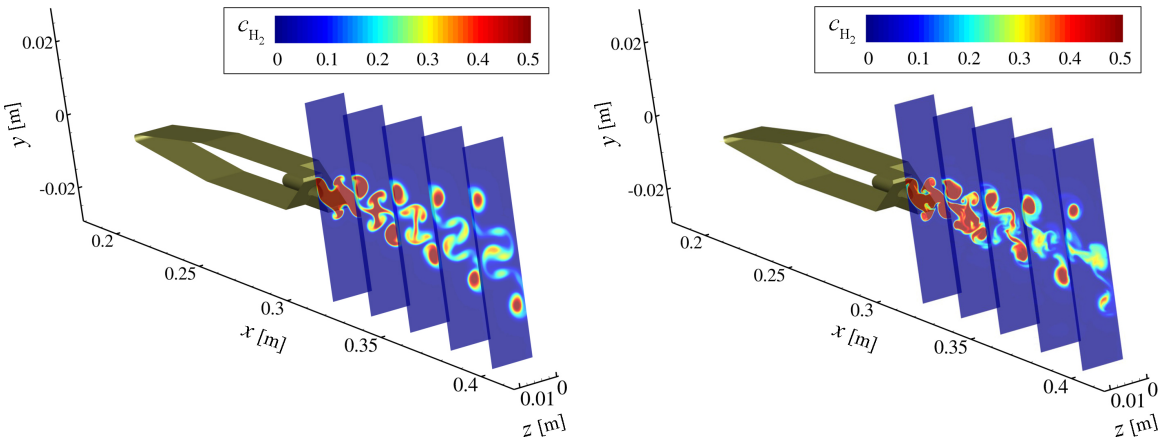

(a) nominal mesh resolution ($\Delta s_{min} = 0.25$ mm)

(b) fine mesh resolution ($\Delta s_{min} = 0.125$ mm)

Fig. 5 Mesh dependency of fuel mass fraction distributions (baseline geometry).

Table 3 Mesh dependency of performance parameters

performance parameter	nominal mesh	fine mesh
η_m	24.5%	21.6%
$\eta_m \times \Phi$	24.6%	21.0%
Δp_0	21.3%	19.1%
$\Delta p_{0\,STA}$	36.7%	34.4%
h_p	11.0 mm	11.0 mm
Γ	27.1 m^2/s	23.5 m^2/s

F. Validation

The flowfields obtained from computational fluid dynamics are compared with experimental results for the validation of the present approaches. For the wind tunnel setup the same configuration as the current one is employed, with the only difference being the streamwise position of the strut (alternating wedges), which is 315 mm downstream of the combustor entrance for the model used in validation whereas it is located 220 mm downstream in the current work. As regards the injector configurations, alternating wedges with two angles, *i.e.*, 22° and 36°, are considered for fuel injection at an equivalence ratio of $\Phi = 0.2$ with the nominal spanwise spacing $s = 1.0$ (11 mm in width). The same modeling method and mesh configurations as what are described previously in this section. Corresponding flowfields were experimentally visualized in a high enthalpy test facility by means of laser diagnosis, in particular, instantaneous Mie scattering in a preceding study[10]. Color scales hence quantitative measurements are not available for the experimental results because of the difference in the output of the laser light hence brightness for each photograph due to the limitation associated with the Mie scattering procedure[10].

Figure 6 compares the distributions of the fuel mass fraction for the ramp angle $\theta = 22°$ obtained numerically for two mesh resolutions (coarse and fine) with the results from the experimental investigation on the $y - z$ planes at 4 streamwise stations, that is, $x' = 10$, 30, 50, and 90 mm, where x' is the relative streamwise coordinate that originates from the trailing edge of the strut. Reasonable agreement can be observed in the streamwise vortex patterns between the computational and experimental flowfields, with a relatively small difference in the extent of the hydrogen

distributions being less than 10%. Vortex structures are resolved more sharply by the simulation with the fine mesh, compared to those by the coarse mesh. Experimental flowfields, on the other hand, are somewhat blurred due possibly to inadequate tracking of the seed particles (SiO_2-based aerosol) or the influence of turbulent diffusion, consequently resulting in fuel distributions somehow resembling those from the computation with the coarse mesh.

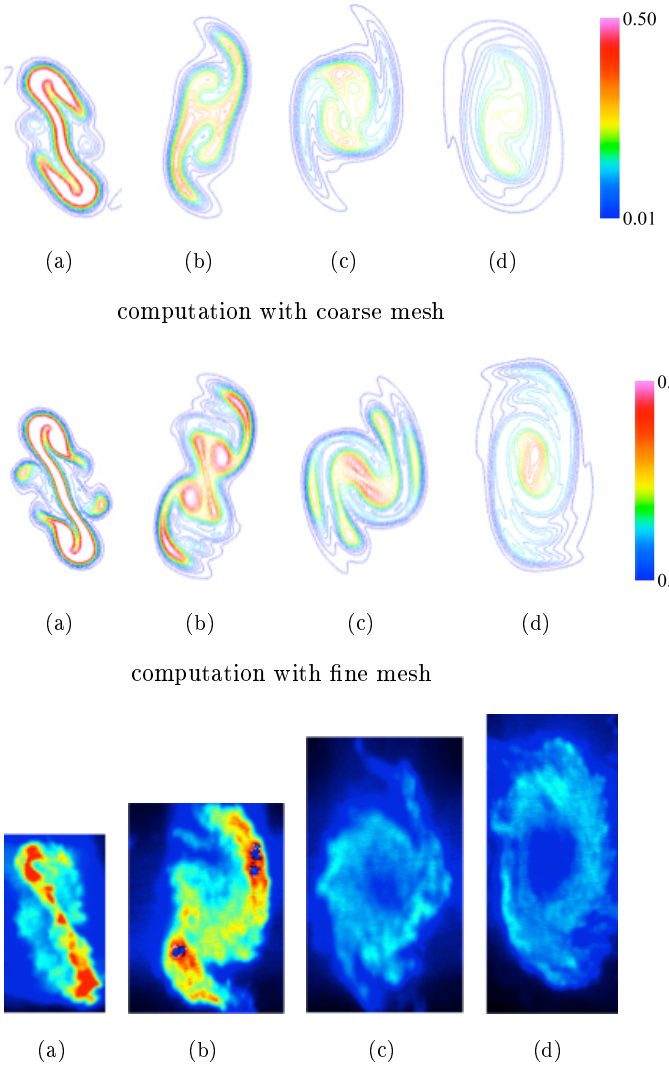

Fig. 6 Comparison of fuel mass fraction distributions on $y-z$ planes at various streamwise stations between computation and experiment (x' = (a) 10 (b) 30 (c) 50 (d) 90 mm, $s = 1.0$, $\theta = 22°$, $\Phi = 0.2$).

Compared in Fig. 7 are the distributions of the fuel mass fraction for the alternating wedge with a ramp angle of $\theta = 36°$ between the computations and experiment on normal planes at 5

streamwise locations, that is, $x' = 5$, 20, 40, 60, and 100 mm. Similar trends to those for $\theta = 22°$ can be seen in that the instantaneous flowfields from Mie scattering visualization bear resemblance to the computed results with the coarse mesh, while streamwise vortices are characterized by similar patterns for all results, particularly in the vicinity of the tailing edge of the strut. However, the difference in the extent of the fuel distributions becomes more pronounced at downstream stations, which may be attributed to increased turbulent effects at higher ramp angles of the strut[20].

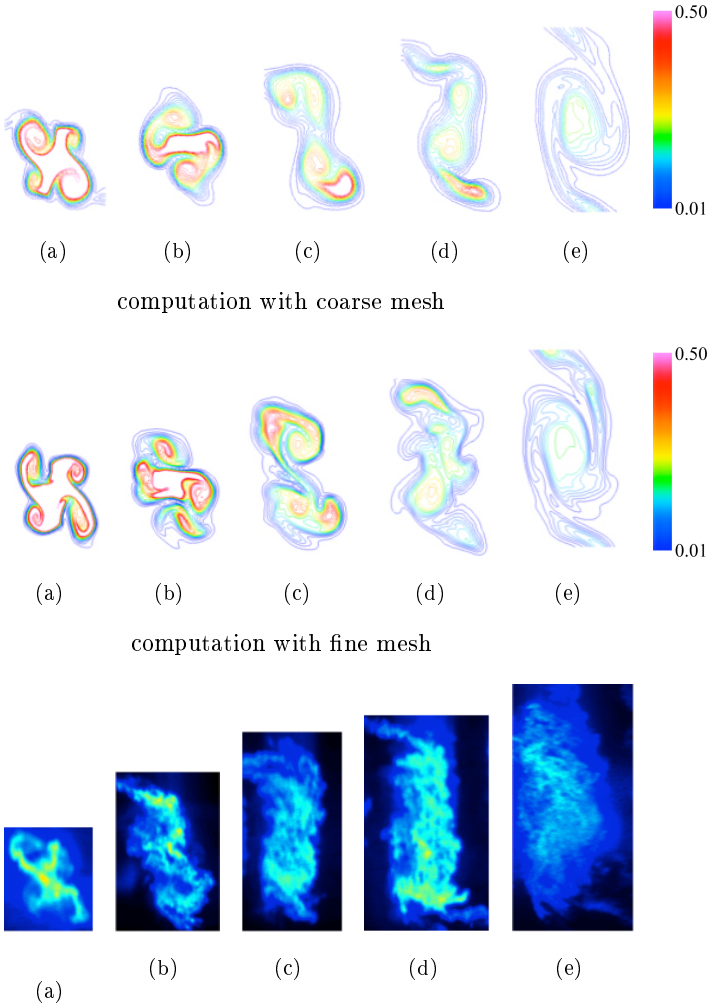

Fig. 7 Comparison of fuel mass fraction distributions on $y-z$ planes at various streamwise stations between computation and experiment (x' = (a) 5 (b) 20 (c) 40 (d) 60 (e) 100 mm, $s = 1.0$, $\theta = 22°$, $\Phi = 0.2$).

On the whole, qualitative agreement is observed with respect to the fuel distributions primarily driven by the streamwise vortices between the experimental investigation and numerical simulations,

where the flow features are captured more sharply with computational grids at a higher resolution (at a considerably higher computational cost, especially for the fine mesh, which is estimated to require at least 10 times longer computational time than the nominal one in consideration of the increase in the mesh size and iteration steps needed for convergence). Based on these observations, in conjunction with the results from the preliminary mesh sensitivity study in the former section, the nominal mesh resolution is employed within the constraints of the resources available for computations in the present study.

G. Parametric study

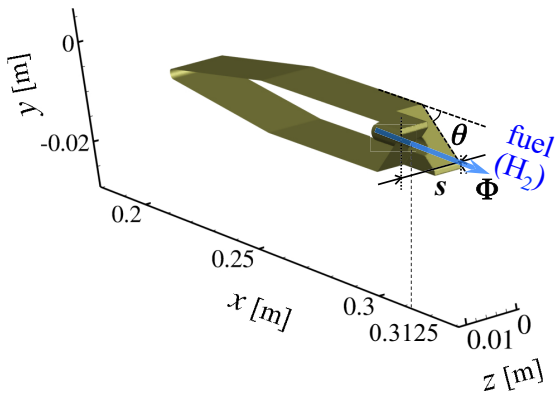

Fig. 8 Parametric representation of hypermixer configuration.

The configuration of the hypermixers is defined by three representative design parameters, as shown in Fig. 8: (a) The spanwise spacing between the adjacent pairs of alternating wedges is represented by the spanwise scaling factor s, which is defined as the ratio of the spacing with respect to the spanwise interval of the baseline geometry, *i.e.*, 11 mm. (b) The ramp angle of the wedges is employed as the second design parameter, denoted as θ. (c) The fuel/air equivalence ratio Φ is used as the third parameter and the injection pressure is adjusted to achieve the intended values of Φ. These parameters are varied within given ranges ($0.5 \leq s \leq 1.5$, $15^\circ \leq \theta \leq 43^\circ$, and $0.2 \leq \Phi \leq 1$) to explore the variations of the performance parameters in response to those in the design parameters.

Five discrete values with equal intervals are taken for each design parameter within these ranges, as shown in Table 4, where bold numbers are indicative of the baseline values. All possible combinations of these values for the design parameters result in 125 computational simulations to be

Table 4 Design parameter values examined in the parametric study

parameter	examined values				
s	0.5	0.75	**1.0**	1.25	1.5
θ	15°	22°	29°	**36°**	43°
Φ	0.2	0.4	0.6	0.8	**1.0**

performed in this study. In varying the ramp angle θ, adjustment is made for the onset of the expansion ramps and the trailing edge of the struts, while the distance from the center of the fuel orifice to the computational domain exit (measurement plane) is maintained constant to be 92.5 mm, with the fuel orifice center anchored at its original streamwise position (*i.e.*, $x = 405$ mm).

H. Sensitivity analysis

Variance-based global sensitivity analysis[25] is performed in order to investigate the impact of each design parameter (s, θ, Φ) on the performance parameter (η_m, $\eta_m \times \Phi$, Δp_0, $\Delta p_{0\,STA}$, h_p, Γ). In particular, a numerical procedure based on Sobol's variance decomposition[26] is employed to derive the sensitivity indices, enabled by surrogate prediction from various meta models such as response surface models, radial basis function networks, kriging and multilayer perceptrons[27]. Input matrices of a base sample number of 10,000 and multiple columns for decision variables (design parameters) are built by using quasi-random numbers[26] within the range for each design parameter described above. Output vectors are obtained by feeding the input matrices into the surrogate model with the best prediction accuracy. The first-order (S_i) and total-effect (S_{T_i}) sensitivity indices, which indicate direct and overall impact of the design parameters, respectively, are calculated by the method outlined in Reference [25].

III. Results

A. Sensitivity analysis

Covariance-based global sensitivity analysis has been performed in order to investigate the influence of the design parameters on the mixing performance of the hypermixer with respect to various criteria described in the previous section. This analysis is performed, based on the surrogate

prediction for the correlation between the design parameters and performance parameters. The minimum root-mean-square errors incurred in the prediction are tabulated in Table 5 along with the surrogate models that have yielded the most accurate prediction with minimum errors for each performance parameter (RSM stands for the response surface model). It can be seen that the prediction errors typically fall within an order of 10%, allowing reasonable qualitative argument.

Table 5 Surrogate prediction errors

performance parameter	rms error	surrogate model
η_m	5.50%	kriging
$\eta_m \times \Phi$	8.65%	kriging
Δp_0	6.38%	RSM
$\Delta p_{0\,STA}$	3.75%	RSM
h_p	8.89%	RSM
Γ	11.2%	kriging

Presented in Fig. 9 is the first-order sensitivity indices S_i and total-effect indices S_{T_i}. They represent the main and overall effect, respectively, of the design parameters (spanwise scaling factor s, ramp angle θ, and fuel/air equivalence ratio Φ) on the performance parameters of interest. The sum of the first-order sensitivity indices is generally smaller than unity ($\Sigma S_i < 1$), whereas that of the total-effect indices is greater than unity ($\Sigma S_{T_i} > 1$). The difference between the total-effect index S_{T_i} and the first-order index S_i is indicative of the degree of the involvement of the decision variable in interactions with other decision variables[25]. It is notable that all performance parameters are largely influenced by two major design parameters, with the third parameter playing a rather minor role, except for θ in η_m and $\eta_m \times \Phi$ and s in Δp_0, which account for sizable influence of 11.4%, 12.5% and 13.5%, respectively.

B. Mixing efficiency

Plotted in Fig. 10 is the contour variation of the mixing efficiency η_m with respect to the spanwise spacing s and fuel/air equivalence ratio Φ, which have been identified as the two dominant parameters for the mixing efficiency. The contours plotted in this section are generated, based on

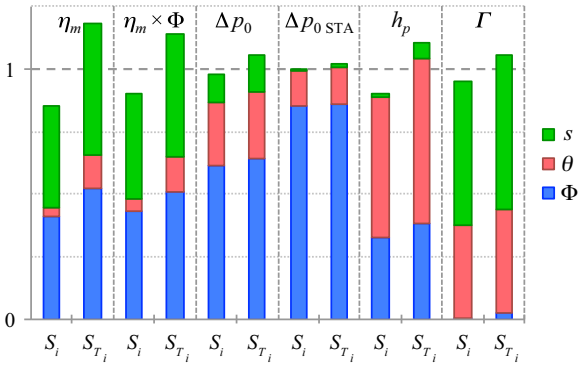

Fig. 9 Sensitivity indices of mixing performance parameters to design parameters.

the cubic interpolation of the results from the CFD simulations, where the color inside the 25 circles represent the average of the 5 solutions with the common abscissa and ordinate values. One can observe a trend where the mixing efficiency decreases as the fuel/air equivalence ratio increases, and narrow spanwise spacing tends to increase the mixing efficiency particularly at lower fuel/air equivalence ratios.

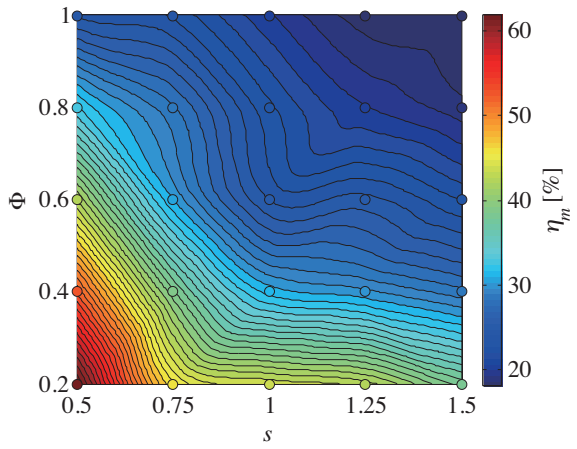

Fig. 10 Mixing efficiency contour plot with respect to spanwise spacing and fuel/air equivalence ratio.

The distributions of the fuel mass fraction at the exit ($x = 405\,\mathrm{mm}$), where the flow distributions presented in this section are plotted unless specified, are compared in Fig. 11 (a) between the fuel/air equivalence ratio of 0.2 and 1.0 with the baseline geometry ($s = 1.0$, $\theta = 36°$), along with the total pressure distributions plotted in Fig. 11 (b) (the plots on the left hand side are mirrored images across $z = 0\,\mathrm{mm}$). Significantly low fuel density is evident in the case of the lower fuel/air equivalence

ratio ($\Phi = 0.2$, left), as compared to $\Phi = 1.0$ (right), while the former has yielded a higher mixing efficiency η_m, as also observed in the sensitivity indices in Fig. 9. Thus η_m does not serve as a useful indicator for the mixing ability for small values of Φ. To address this issue, the absolute mixing quantity, defined as the product of the mixing efficiency and the fuel/air equivalence ratio, is examined in order to enable the comparison of the mixing performance accounting for the difference in the fuel/air equivalence ratio.

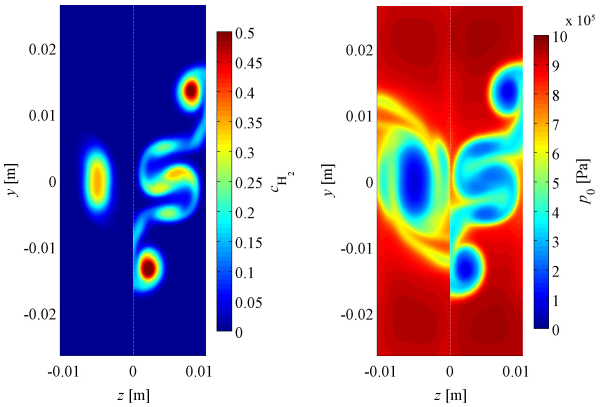

(a) fuel mass fraction (b) total pressure

Fig. 11 Comparison of fuel mass fraction and total pressure distributions ($s = 1.0$, $\theta = 36°$, Φ = left: 0.2 | right: 1.0).

Figure 12 shows the variation of the absolute mixing quantity $\eta_m \times \Phi$ with respect to the spanwise spacing and fuel/air equivalence ratio. It suggests that larger absolute mixing quantity is achieved by smaller spanwise spacing and larger fuel/air equivalence ratio (the latter of which is a matter of course by definition), particularly at large fuel/air equivalence ratios. The comparison of the fuel mass fraction distributions plotted in Fig. 13 (a) indeed indicates more uniform fuel/air mixture with $s = 0.5$ (left) than with $s = 1.5$ (right), where hydrogen with intense density concentration is enclosed in a pair of strong streamwise vorticity domains (Fig. 13 (b), right). These results suggest that intense fluid entrainment owing to strong vorticity generation does not necessarily contribute to mixing enhancement but can result in isolation of highly concentrated fuel cores.

In order to scrutinize the underlying mechanism of the trend observed above, the progression of fuel/air mixing is visualized and compared between the geometries with the minimum and maximum spanwise spacing in Figs. 14 and 15. In the case of the narrow spanwise spacing, it can be seen that

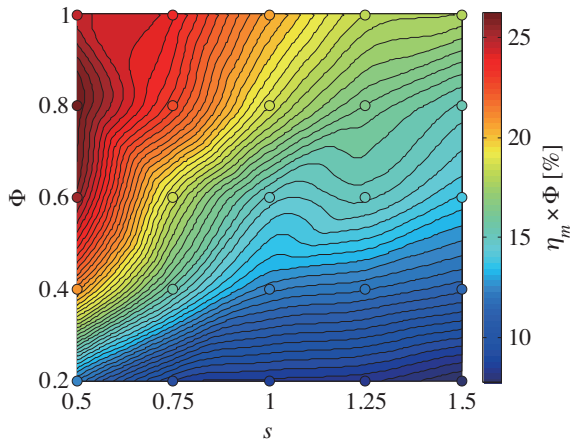

Fig. 12 Absolute mixing quantity contour plot with respect to spanwise spacing and fuel/air equivalence ratio.

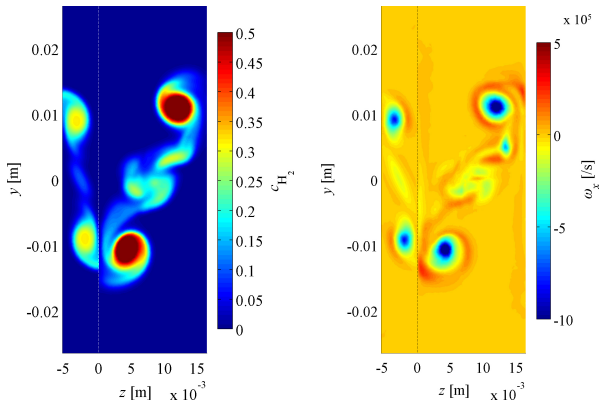

(a) fuel mass fraction

(b) streamwise vorticity

Fig. 13 Comparison of fuel mass fraction and streamwise vorticity distributions (s = left: 0.5 | right: 1.5, $\theta = 36°$, $\Phi = 1.0$).

both fuel and air are captured in the swirling vortices ($x = 350 - 380$ mm, Fig. 14 (a)) and mixing is promoted owing to the vorticity present in the same regions (Fig. 14 (b)). The wide spanwise spacing, on the other hand, is characterized by the existence of highly concentrated fuel cores, which are formed at an early stage of mixing ($x = 340$ mm, Fig. 15 (a)). These can be assumed to be generated by strong swirls, which interact with their counterparts across the symmetry planes at $z = 11$ and 0 mm, resulting in upward and downward motions, respectively. Fuel/air mixing is little promoted in this fuel core pair, which predominantly comprises hydrogen from the onset of their

formation, consequently yielding rather poor mixing efficiency despite large streamwise vortices.

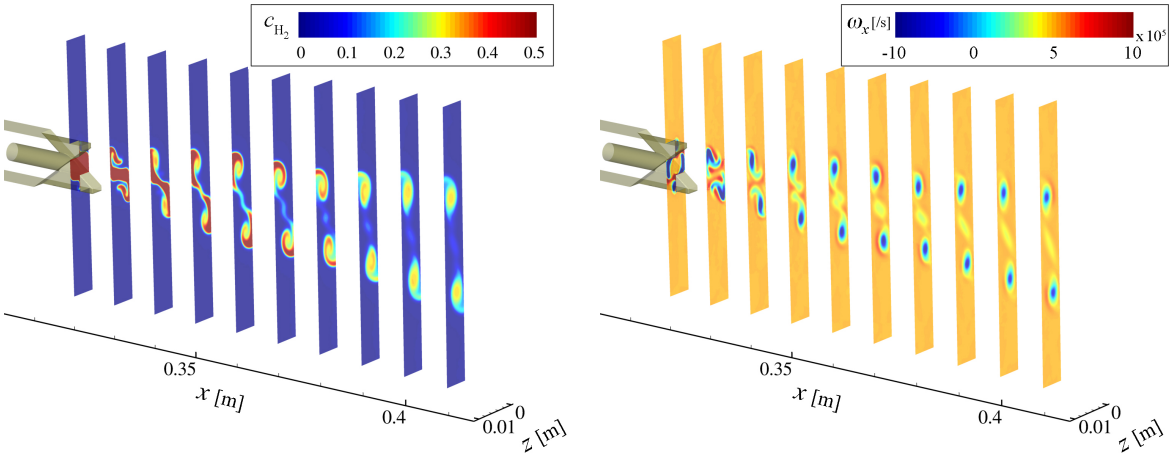

(a) fuel mass fraction (b) streamwise vorticity

Fig. 14 Flowfield progression plotted on planes at $x = 315 - 415$ mm with 10 mm intervals ($s = 0.5$, $\theta = 36°$, $\Phi = 1.0$).

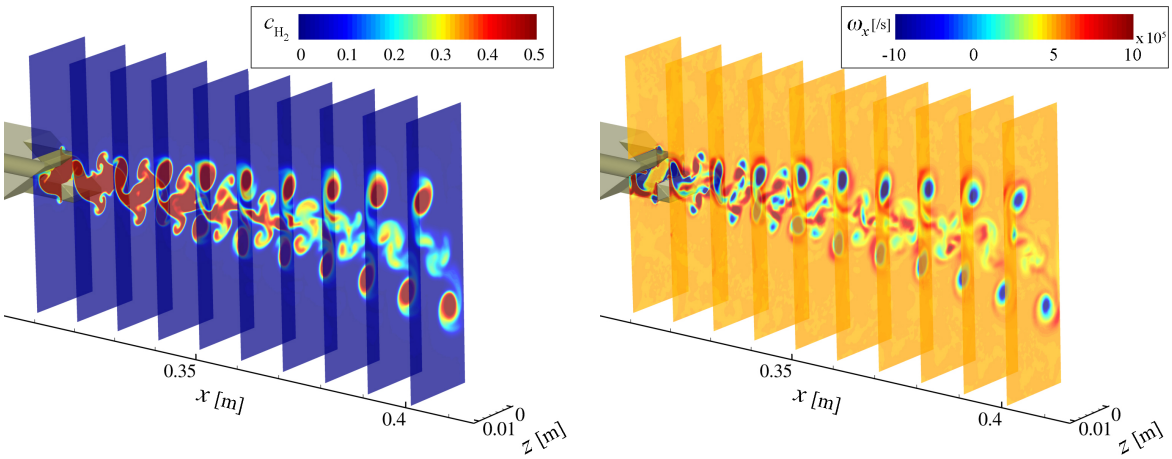

(a) fuel mass fraction (b) streamwise vorticity

Fig. 15 Flowfield progression plotted on planes at $x = 315 - 415$ mm with 10 mm intervals ($s = 1.5$, $\theta = 36°$, $\Phi = 1.0$).

The dependency of the absolute mixing quantity on the ramp angle θ, which has been assumed to have rather minor influence on this quantity in the sensitivity analysis (Fig. 9), is examined in Fig. 16. The contour plot, on the contrary, suggests considerable influence of θ particularly at higher fuel/air equivalence ratios, whereas it exerts indiscernible impact at lower equivalence ratios. This compound reliance observed here has presumably resulted in greater total-effect sensitivity index

S_{T_i} of θ than the first-order index S_i (Fig. 9), which is a measure of the direct role solely played by θ.

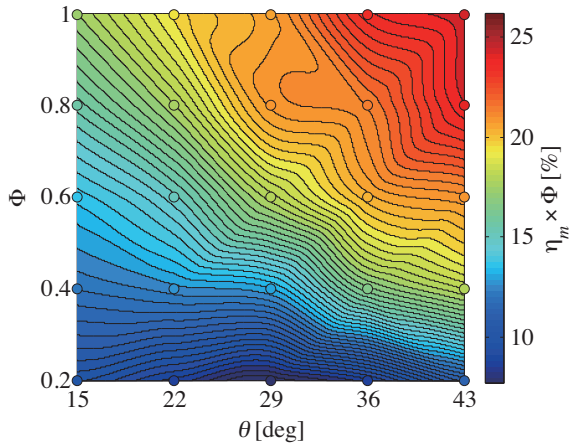

Fig. 16 Absolute mixing quantity contour plot with respect to ramp angle and fuel/air equivalence ratio.

C. Total pressure loss

The contour variations of the total pressure losses based on mass-weighted and stream-thrust averaging are plotted in Figs. 17 and 18, respectively, with respect to the two major parameters, namely, the ramp angle θ and fuel/air equivalence ratio Φ. Both averaging methods commonly indicate larger total pressure losses with greater ramp angles and larger fuel/air equivalence ratios, while the stream-thrust averaged loss (Fig. 18) indicates higher sensitivity of the total pressure loss to Φ than to θ according to the contour gradients, in concordance with the sensitivity indices plotted in Fig. 9.

The dependency of the total pressure distributions on the fuel/air equivalence ratio Φ is exemplified in Fig. 11 (b), where regions of high fuel density intrinsically correspond with those of low total pressure. The total pressure distributions with the two extreme ramp angles ($\theta = 15°$ and 43°) are compared in Fig. 19 along with the streamwise vorticity distributions. Corresponding distributions of the fuel mass fraction are plotted in Fig. 20 (a). Resemblance is generally observed between the total pressure distributions (Fig. 19 (a)) and the streamwise vorticity distributions (Fig. 19 (b)) for both angles. On the other hand the low total pressure region inside the core vortex in

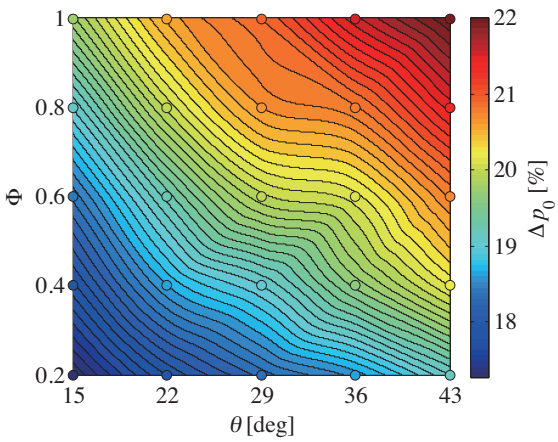

Fig. 17 Total pressure loss contour plot with respect to ramp angle and fuel/air equivalence ratio.

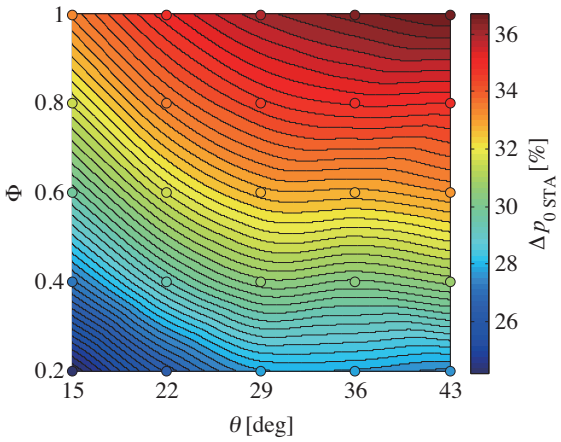

Fig. 18 Stream-thrust-averaged total pressure loss contour plot with respect to ramp angle and fuel/air equivalence ratio.

the middle at $\theta = 43°$ appears to correspond with the high fuel density region (Fig. 20 (a)).

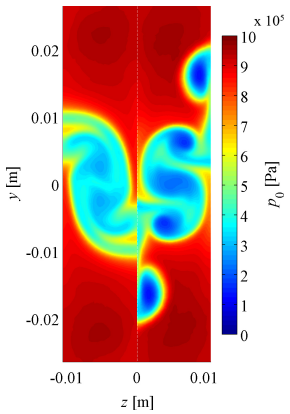

(a) total pressure

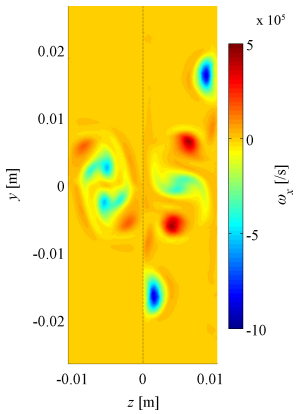

(b) streamwise vorticity

Fig. 19 Comparison of total pressure and streamwise vorticity distributions ($s = 1.0$, $\theta =$ left: $15°$ | right: $43°$, $\Phi = 1.0$).

Figure 21 displays the variation of the total pressure distributions with various values of spanwise spacing, while the ramp angle and fuel/air equivalence ratio are maintained at constant values ($\theta = 36°$, $\Phi = 1.0$). These plots indicate that the pattern of low total pressure regions remains relatively unaffected by the change in the spanwise scaling factor s on the whole. The pattern

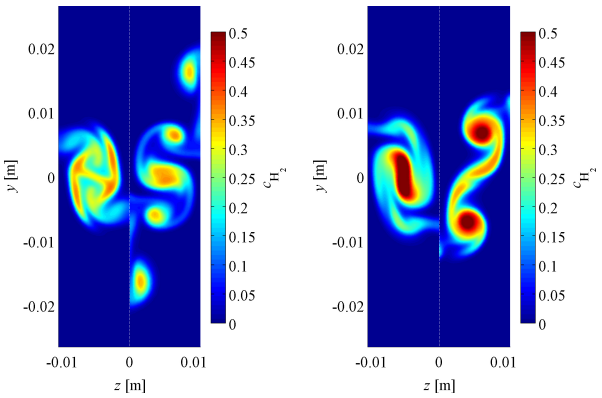

(a) θ = left: 15° | right: 43°

(b) θ = left: 22° | right: 29°

Fig. 20 Fuel mass fraction distributions ($s = 1.0$, $\Phi = 1.0$).

shrinks or stretches in the spanwise direction according to s, accompanied by the increase in the area of the high total pressure (close to the freestream value) in proportion, except for $s = 0.5$, where the pattern contracts in the vertical direction as well. This may well be the reason why the spanwise scaling factor s has been judged to be the least influential parameter on the total pressure loss as a result of the sensitivity analysis, as seen in Fig. 9.

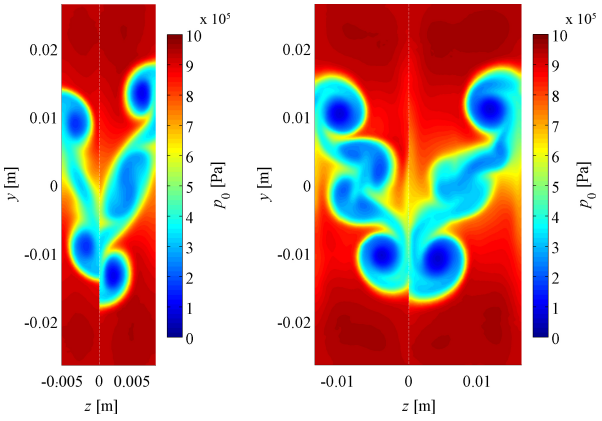

(a) s = left: 0.5 | right: 0.75

(b) s = left: 1.25 | right: 1.5

Fig. 21 Total pressure distributions ($\theta = 36°$, $\Phi = 1.0$).

D. Fuel penetration height

Plotted in Fig. 22 is the contour variation of the maximum fuel penetration height h_p, which has been found to be largely dictated by the ramp angle θ and fuel/air equivalence ratio Φ according to the sensitivity analysis. Its dependency on Φ has already been seen in Fig. 11 (a), where a smaller fuel/air equivalence ratio ($\Phi = 0.2$, left) has resulted in a small patch with low fuel density and therefore a lower penetration height. Figure 20 (a) has highlighted the crucial influence on the fuel penetration pattern induced by the ramp angle. The fuel mass fraction distributions for $\theta = 22°$ and 29° are plotted additionally in Figure 20 (b). It is notable that the $\theta = 43°$ case is characterized by a distinctly different fuel pattern than the other angles, featuring a secondary streamwise vortex pair located distantly from the main vortices. This isolated vortex pair has resulted in the higher sensitivity of h_p to θ at large Φ values.

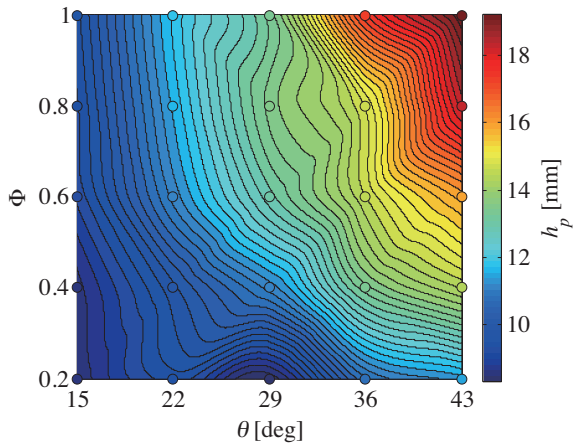

Fig. 22 Fuel penetration height contour plot with respect to ramp angle and fuel/air equivalence ratio.

The progression of fuel/air mixing is visualized for the two extreme ramp angles in Figs. 23 and 24 in order to investigate the driving force dictating the formation of the fuel patterns observed above. In the case of the shallow ramp angle, the major portion of the fuel remains in the vicinity of the centerline downstream of the injector orifice and gently stirred by relatively mild streamwise vortices (Fig. 23). The steep ramp angle, on the other hand, provokes abrupt swirls, whose momentum is strong enough to wrench off both ends of the fuel stream, in conjunction with the interactions on the symmetry planes at $z = 11$ and 0 mm. The resultant vortices mutually promote

their upward and downward motion at $z = 11$ and 0 mm, respectively, across the symmetry planes (Fig. 24), conducing to greater fuel penetration. However, the fuel confined inside these vortices are gradually mixed with the air across the contact surface in this movement. It consequently leads to relatively high mixing efficiency but larger total pressure loss, as observed in Fig. 19 (a).

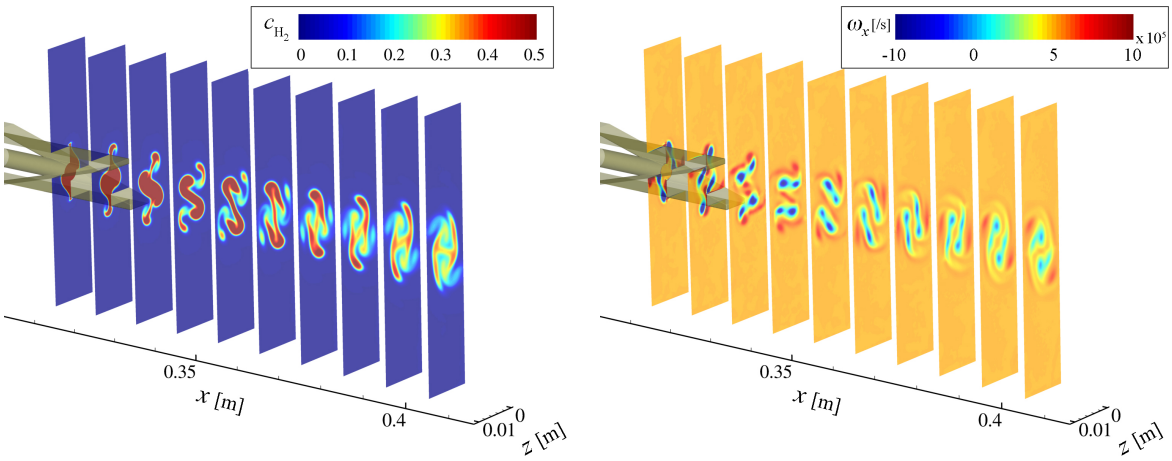

(a) fuel mass fraction (b) streamwise vorticity

Fig. 23 Flowfield progression on planes at $x = 315 - 415$ mm ($s = 1.0$, $\theta = 15°$, $\Phi = 1.0$).

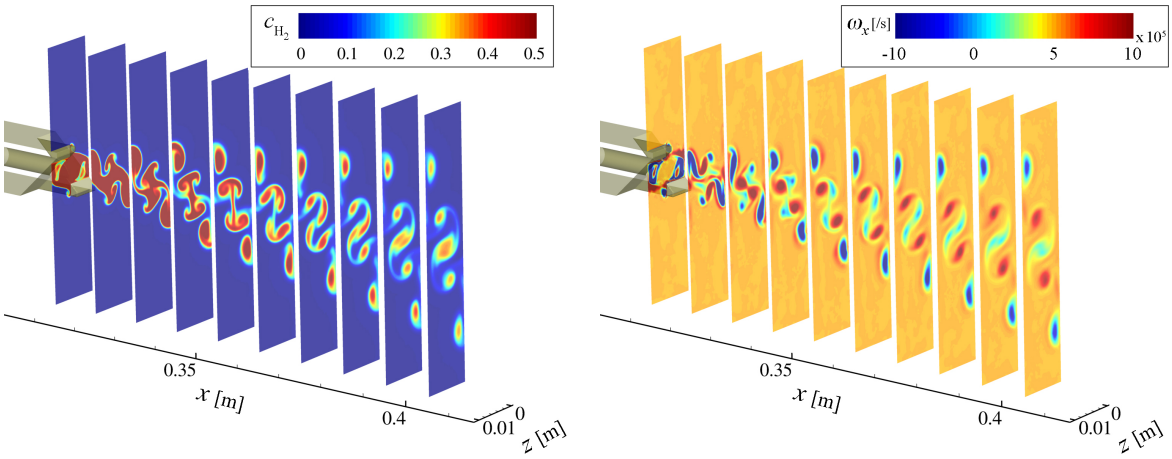

(a) fuel mass fraction (b) streamwise vorticity

Fig. 24 Flowfield progression on planes at $x = 315 - 415$ mm ($s = 1.0$, $\theta = 43°$, $\Phi = 1.0$).

The contours in Fig. 22 also suggest that h_p becomes rather independent of Φ at low ramp angles θ, where streamwise vortices do not cause broad spread of the fuel in the vertical direction, as seen in the fuel distributions plotted in Fig. 25 (a) for $\theta = 15°$ in stark contrast to Fig. 25 (b) for

$\theta = 43°$, where a highly elongated fuel distribution can be seen at $\Phi = 0.6$. The insensitivity of the fuel penetration height to the spanwise spacing has been seen in Fig. 13 (a).

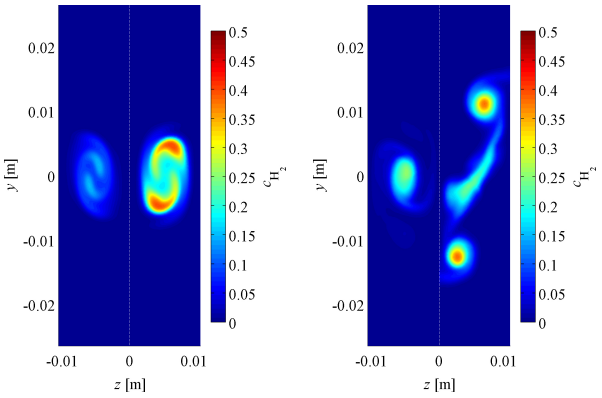

(a) $\Phi =$ left: 0.2 | right: 0.6

(b) $\Phi =$ left: 0.2 | right: 0.6

Fig. 25 Comparison of fuel mass fraction distributions ($s = 1.0$, (a) $\theta = 15°$ | (b) $\theta = 43°$).

E. Streamwise vortex circulation

The variation of the streamwise vortex circulation Γ is presented in Fig. 26 with respect to its two dominant parameters, namely, the spanwise spacing s and ramp angle θ. It is notable that the circulation tends to rise with the increase of the spanwise spacing and ramp angle, but it peaks at a certain combination near $s = 1.35$ and $\theta = 37°$, suggesting the presence of an optimum geometry with regards to the streamwise vortex circulation, while it does not necessarily ensure the optimum mixing in the present assumptions, as discussed formerly. The variations of the streamwise vorticity distributions according to the spanwise spacing and ramp angle have been plotted in Fig. 13 (b) and Fig. 19 (b), respectively.

The distributions of the streamwise vorticity with various values of the fuel/equivalence ratio Φ are displayed in Fig. 27. It is interesting to note that Φ has negligible influence on the streamwise vortex circulation according to the sensitivity indices in Fig. 9 in spite of the considerable variations of the streamwise vorticity distributions observed in these plots.

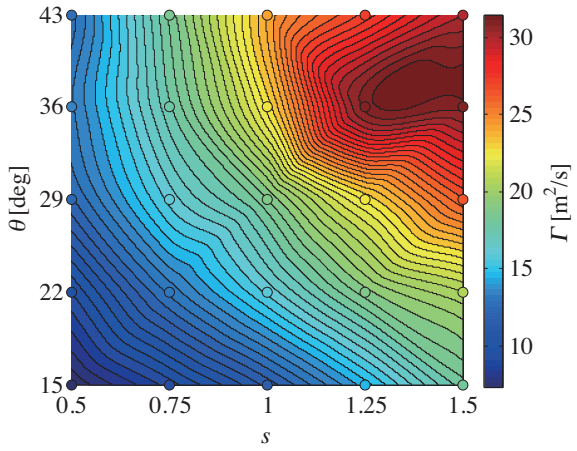

Fig. 26 Streamwise circulation contour plot with respect to spanwise spacing and ramp angle.

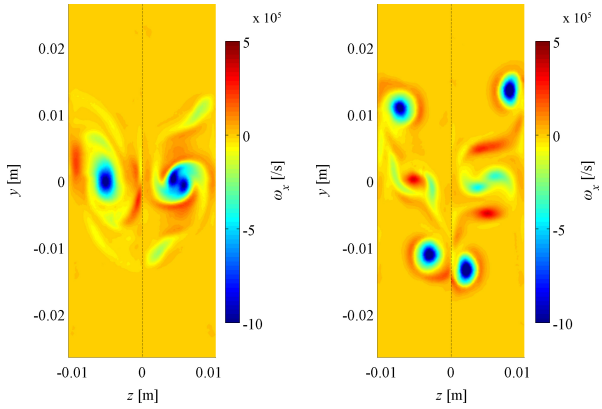

(a) Φ = left: 0.4 | right: 0.6

(b) Φ = left: 0.8 | right: 1.0

Fig. 27 Streamwise vorticity distributions ($s = 1.0$, $\theta = 36°$).

F. Summary

The general effects of the three design parameters on the six performance parameters are summarized in Table 6, based on the knowledge obtained as a result of the observations made in this section (favorable characteristics are indicated by asterisks).

IV. Conclusions

A numerical investigation has been conducted for the fuel/air mixing via streamwise vortices generated by the hypermixers comprising a row of alternating wedges with central fuel injection, aiming at an application to the combustor of scramjet engines. A parametric study with three-

Table 6 Summary of major influence of design parameters on mixing performance

		η_m	$\eta_m \times \Phi$	Δp_0	$\Delta p_{0\,STA}$	h_p	Γ
s	↗	↘	↘	→	→	→	↗*
	↘	↗*	↗*	→	→	→	↘
θ	↗	↗*	↗*	↗	↗	↗*	↗*
	↘	↘	↘	↘*	↘*	↘	↘
Φ	↗	↘	↗*	↗	↗	↗*	→
	↘	↗*	↘	↘*	↘*	↘	→

dimensional computational simulations have been performed to examine the flowfields resulting from various combinations of the three design parameters, that is, the spanwise spacing and ramp angle of the alternating wedges, and the fuel/air equivalence ratio.

Performance parameters for the mixing efficiency, total pressure loss, fuel penetration height, and streamwise vortex circulation have been calculated by processing the flow properties at the exit of the computed domain. Sensitivity analysis based on surrogate prediction has been applied to these results in order to identify the two dominant design parameters for each performance parameter.

The following knowledge has been gained into the roles played by the design parameters in fuel mixing:

- Narrow spanwise spacing is favorable to achieve efficient fuel/air mixing (based on the absolute mixing quantity), whereas wider spacing can induce strong streamwise vortex circulation, but does not help improve mixing performance.

- Steeper ramp angles enable fuel to propagate to greater vertical height and augment streamwise vortex circulation, which contributes to higher mixing efficiencies in this case, but milder angles are preferable to avoid large total pressure loss.

- Larger fuel/air equivalence ratio conduces to greater absolute mixing quantity (by definition) and higher fuel penetration, but inherently incurs larger total pressure loss due to larger proportion of fuel present in the mixed gas.

- Streamwise vortices can effectively enhance fuel/air mixing if air is entrained into the incipient

vortices in their formation process, but otherwise intensely strong vorticity rather confines highly concentrated fuel cores, contributing little to mixing.

- The vortex interactions across the symmetry planes play an active role in convective mixing because the neighboring vortices mutually act on each other, promoting vertical motions, impacting on the mixing characteristics significantly.

The above conclusions have been drawn within the limited conditions used in the present study (*i.e.*, no turbulence model, no chemical reactions). However, they provide useful insight into the key design parameters for mixing enhancement as well as the mixing process that is purely driven by the aerodynamic interactions between the fuel and air.

Acknowledgements

The authors are grateful to Prof. R. R. Boyce for providing resources in this research project during the appointments at the Centre for Hypersonics, The University of Queensland, as well as to the MDO Group led by Dr. Tapabrata Ray at UNSW Canberra for the capability of surrogate modeling used in the present study. They are also thankful to Dr. T. Sunami at JAXA Kakuda Space Center for his invaluable advice. They wish to acknowledge the support of the Australian Research Council through the DECRA (Discovery Early Career Researcher Award) Grant No. DE120102277 for Dr. Ogawa. They also acknowledge the use of the JAXA Supercomputer System (JSS), on which the numerical simulations presented in this paper have been performed.

References

[1] Paull, A., Alesi, H., and Anderson, S., "HyShot Flight Program and How it was Developed", AIAA Paper 2002-5248, Sep 2002.

[2] McClinton, C. R., "X-43 – Scramjet Power Breaks the Hypersonic Barrier: Dryden Lectureship in Research for 2006", AIAA Paper 2006-1-317, Jan 2006.

[3] Mutzman, R., and Murphy, S., "X-51 Development: A Chief Engineer's Perspective", 17th AIAA International Space Planes and Hypersonic Systems and Technologies Conference San Francisco, CA, Apr 2011.

[4] Boyce, R. R., Tirtey, S. C., Brown, L., Creagh, M., and Ogawa, H., "SCRAMSPACE : Scramjet-based Access-to-Space Systems", AIAA Paper 2011-2297, Apr 2011.

[5] Steelant, J., "Achievements obtained for sustained hypersonic flight within the LAPCAT project", AIAA Paper 2008-2578, Apr-May 2008.

[6] McGuire, J. R., Boyce, R. R., and Mudford, N. R., "Radical Farm Ignition Processes in Two-Dimensional Supersonic Combustion", *Journal of Propulsion and Power*, Vol. 24, No. 6, 2008, pp.1248-1257.

[7] Wendt, M. N. and Stalker, R. J., "Transverse and Parallel Injection of Hydrogen with Supersonic Combustion in a Shock Tunnel", *Shock Waves*, Vol. 6, 1996, pp. 53-59.

[8] Wheatley, V. and Jacobs, P. A., "Fuel Injection via Rectangular Cross-section Injectors for Mixing Enhancement in Scramjets", 17^{th} Australasian Fluid Mechanics Conference, Auckland, New Zealand, Dec 2010.

[9] Sunami, T., Nishioka, M., Murakami, A., Kudoh, K., and Wendt, M. N., "Alternating-Wedge Strut Injection for Supersonic Mixing and Combustion", 14^{th} International Symposium on Airbreathing Engines, Florence, Italy, Sep 1999.

[10] Sunami, T. and Scheel, F., "Analysis of Mixing Enhancement Using Streamwise Vortices in a Supersonic Combustor by Application of Laser Diagnostics", AIAA Paper 2002-5203, Sep-Oct 2002.

[11] Sunami, T. and Scheel, F., "Observation of Mixing and Combustion Process of H_2 Jet Injected into Supersonic Streamwise Vortices", *Shock Waves*, Springer-Verlag Berlin Heidelberg, 2005, pp. 921-926.

[12] Capra, B. R., Boyce, R. R., and Brieschenk, S., "Numerical Modelling of Porous Injection in a Radical Farming Scramjet", ICAS Paper 2012-4.11.1, Sep 2012.

[13] Riggins, D. W. and McClinton, C. R., "Analysis of Losses in Supersonic Mixing and Reacting Flows", AIAA Paper 91-2266, Jul 1991.

[14] Riggins, D. W., McClinton, C. R., and Vitt, P. H., "Thrust Losses in Hypersonic Engines Part 1: Methodology", *Journal of Propulsion and Power*, Vol. 13, No. 2, 1997, pp. 281-287.

[15] Stalker, R. J., Paull, A., Mee, D. J., Morgan, R. G., and Jacobs, P. A., "Scramjets and Shock Tunnels – The Queensland Experience", *Progress in Aerospace Sciences*, Vol. 41, 2005, pp.471-513.

[16] Waitz, I. A., Qiu, Y. J., Manning, T. A., Fung, A. K. S., Elliot, J. K., Kerwin, J. M., Krasnodebski, J. K., O'Sullivan, M. N., Tew, D. E., Greitzer, E. M., Marble, F. E., Tan, C. S., and Tillman, T. G., "Enhanced Mixing with Streamwise Vorticity", *Progress in Aerospace Sciences*, Vol. 33, pp.323-351, 1997.

[17] Kodera, M., Sunami, T. and Nakahashi, K., "Numerical Analysis of Scramjet Combusting flows by

Unstructured Hybrid Grid Method", AIAA Paper 2000-0886, Jan 2000.

[18] Yoon, S. and Jameson, A., "Lower-Upper Symmetric-Gauss-Seidel Method for the Euler and Navier-Stokes Equations", *AIAA Journal*, Vol. 26, No. 9, 1988, pp. 1025-1026.

[19] Wada, Y. and Liou, M.-S., "A Flux Splitting Scheme with High-Resolution and Robustness for Discontinuities", AIAA Paper 94-0083, Jan 1994.

[20] Kodera, M., Sunami, T., and Scheel, F., "Numerical Study on the Supersonic Mixing Enhancement Using Streamwise Vortices", AIAA Paper 2002-5117, Sep-Oct 2002.

[21] Pointwise, *Software Package*, Ver. 16.02, Pointwise, Inc., TX, 2008.

[22] MEGG3D (Mixed-Element Grid Generator in 3 Dimensions), *Software Package*, Ver. 6.1.0.1, Copyright © Japan Aerospace Exploration Agency, 2012.

[23] Kodera, M. and Sunami, T., "Numerical Study on the Hyper-Mixer Fuel Injector for Scramjet Engines", *Proceedings of International Workshop on Future of CFD and Aerospace Sciences*, 2012, Kobe, Japan.

[24] Heiser, W. H. and Pratt, D. T., "Hypersonic Airbreathing Propulsion", *AIAA Education Series*, AIAA, New York, 1994, pp. 447-451.

[25] Saltelli, A., Ratto, M., Andres, T., Compolongo, F., Cariboni, J., Gatelli, D., Saisana, M., and Tarantola, S., *Global Sensitivity Analysis. The Primer*, Wiley, England, 2008.

[26] Sobol, I. M., "Uniformly distributed sequences with additional uniformity properties", *U.S.S.R. Computational Mathematics and Mathematical Physics*, Vol. 16, No. 5, 1976, pp. 236-242

[27] Queipo, N. V., Haftka, R. T., Shyy, W., Goel, T., Vaidyanathan, R., and Tucker, P. K., "Surrogate-Based Analysis and Optimization", *Progress in Aerospace Sciences*, Vol. 41, 2005, pp.1-28.